

## Direct Observation of Chemical Short-Range Order in CoCrNi Alloy Using Neutron Diffraction

Vinicius P. Bacurau<sup>a,b</sup>, Camilo Salvador<sup>c</sup>, Guilherme C. Stumpf<sup>a,b</sup>, Angelo F. Andreolli<sup>a</sup>, Caroline B. Stoco<sup>a,b</sup>, Eric M. Mazzer<sup>a,b</sup>, Lewis Owen<sup>d</sup>, Yifan Cao<sup>e</sup>, Rodrigo Freitas<sup>e</sup>, Daniel Miracle<sup>f</sup>, Francisco G. Coury<sup>a,b</sup>

<sup>a</sup>*Department of Materials Engineering, Federal University of São Carlos (UFSCar), São Carlos, Brazil*

<sup>b</sup>*Graduate Program in Materials Science and Engineering, Federal University of São Carlos, São Carlos, São Paulo, Brazil*

<sup>c</sup>*Université Paris-Saclay, CEA, Service de recherche en Corrosion et Comportement des Matériaux, SRMP, 91191 Gif Sur Yvette, France*

<sup>d</sup>*Department of Materials Science and Engineering, University of Sheffield, Sheffield, United Kingdom*

<sup>e</sup>*Department of Materials Science and Engineering, Massachusetts Institute of Technology, Cambridge, MA, USA*

<sup>f</sup>*AF Research Laboratory, Materials and Manufacturing Directorate, Wright-Patterson AFB, OH, USA*

Corresponding authors at: *Department of Materials Engineering, Federal University of São Carlos (UFSCar), São Carlos, Brazil, Graduate Program in Materials Science and Engineering, Federal University of São Carlos, São Carlos, São Paulo, Brazil*

Corresponding authors

E-mail addresses: fgcoury@ufscar.br (F.G Coury) and vinicius.bacurau@estudante.ufscar.br (V.P. Bacurau)

Abstract:

This study provides experimental evidence of chemical short-range order (CSRO) in the equiatomic CoCrNi alloy, identified through neutron diffraction. The phenomenon manifests as a distinct diffuse peak at  $Q \approx 1.85 \text{ \AA}^{-1}$ , the intensity increases under thermodynamically favorable conditions for CSRO development such as prolonged aging (100 h and 240 h) at 748 K or shorter aging (24 h) at slightly higher temperature (798 K). The degree of ordering was measured by integrating the diffuse scattering intensity, revealing that the gas-atomized sample, i.e. the sample with the least amount of CSRO, still displays approximately 70% of the CSRO level observed in the sample subsequently aged for 240 h at 748 K, i.e. the sample with the highest amount of CSRO produced in this study. Predictive atomistic simulations reproduced both the presence and position of the diffuse peak, while two-dimensional fast Fourier transform (FT-2D) analyses indicated that reflections at  $(1 \frac{1}{2} 0)$  within the  $\langle 001 \rangle$  zone axis originate from some structural projections associated with like  $D0_{22}$ ,  $Pt_2Mo$  and  $D1a$  motifs. Complementary small-angle neutron scattering (SANS) measurements identified Ni-rich, disk-shaped domains with radii of approximately 11 Å and thicknesses of about 1 Å, consistent with nanoscale CSRO characteristic length scale. These findings demonstrate that CSRO is an intrinsic and energetically favorable feature of the CoCrNi system, remaining stable even under rapid solidification and further enhanced by low-temperature aging. Combined use of neutron diffraction and atomistic modeling provides a framework for probing local ordering phenomena in multi-principal element alloys (MPEAs).

Keywords: CoCrNi, Chemical Short-Range Order, Neutron diffraction, SANS

### 1. Introduction

The development of multi-principal element alloys (MPEAs) has sparked interest in understanding their local atomic configurations, particularly the phenomenon of chemical short-range order (CSRO) [1–5]. Among these alloys, the equiatomic CoCrNi solid solution has emerged as a model system due to its exceptional mechanical properties and microstructural stability at cryogenic and ambient temperatures [6–8].

CSRO refers to the non-random arrangement of atoms in a lattice within a few nearest-neighbor shells in otherwise chemically disordered solid solutions. While its presence is well established in conventional binary alloys [9–12], its detection in concentrated multicomponent systems remains challenging, especially when the

constituent elements are adjacent in the periodic table and exhibit limited scattering or weak contrast in conventional X-ray or electron-based techniques [13–15].

Several studies have reported the detection of CSRO through diffuse peaks observed in transmission electron microscopy (TEM) diffraction patterns [3,4,14]. However, Coury et al. [16] demonstrated that many of the diffuse reflections commonly attributed to ordering phenomena in selected area electron diffraction (SAED) patterns of face-centered cubic (FCC) alloys may actually originate from higher-order Laue zones. This finding highlights the importance of caution when interpreting CSRO signatures based solely on electron diffraction.

Along similar lines, Walsh *et al.* [17] reported that features historically identified as indicators of CSRO in FCC alloys may instead originate from alternative mechanisms, including thermal and static atomic displacements, lattice vibrations, and strain fields, as well as secondary effects such as planar defects, surface contributions, and dynamic scattering. These factors can generate diffuse spots that mimic CSRO, reducing the reliability of electron diffraction as a primary tool for detecting CSRO.

The selection of an appropriate diffraction technique to accurately detect chemical order or disorder is strongly dependent on the alloy composition, as the ideal radiation source is the one that provides the highest contrast between the constituent elements.

In the case of equiatomic CrCoNi, widely regarded as a benchmark system for CSRO studies, the atomic numbers of Cr, Co, and Ni are very similar (24, 27, and 28 electrons, respectively). As a result, X-ray and electron diffraction techniques lack sufficient contrast to reliably distinguish between these elements, rendering them ineffective for detecting CSRO in this alloy [15]. In contrast, neutron diffraction offers a clear advantage. The coherent neutron scattering lengths of Cr, Co, and Ni differ significantly (3.64 fm, 2.49 fm, and 10.3 fm, respectively), providing enhanced chemical sensitivity. This increased contrast enables the detection of subtle features associated with chemical short-range order.

These limitations have driven the search for more robust approaches to identify and measure CSRO in CrCoNi. In this context, neutron diffraction has emerged as a particularly suitable technique, owing to the weak dependence of neutron scattering lengths on atomic number and the resulting improvement in chemical contrast among the constituent elements[18].

To overcome these challenges, Bacurau et al. [5] combined high-precision differential scanning calorimetry and machine-learning-assisted atomistic simulations to unambiguously detect and quantify CSRO in CoCrNi and CrNi<sub>2</sub> alloys. Their methodology allowed not only the identification of CSRO states with high sensitivity but also the estimation of the enthalpy associated with CSRO formation and dissolution. Notably, they showed that even in the absence of long-range order, significant changes in calorimetric response could be attributed to local ordering transitions.

CSRO in equiatomic CrCoNi has also been investigated through extended X-ray absorption fine structure (EXAFS) and pair distribution function (PDF) analyses [13,19,20]. Spin-polarized DFT (density functional theory) simulations [21] have suggested that magnetic interactions may drive the tendency to avoid Cr–Cr nearest neighbor pairs. Furthermore, studies on binary Ni–Cr alloys with dilute Cr content have revealed the presence of diffuse neutron scattering at half-integer positions such as  $(1 \frac{1}{2} 0)$ , consistent with the development of short-range order involving Cr avoidance in first-neighbor shells. Interestingly, however, this does not correspond to the typical long-range ordered phases observed for Ni–Cr systems [22].

Despite these improvements, the literature still lacks a direct and consistent measure of CSRO levels in CrCoNi across distinct processing conditions. To date, no study has unambiguously established the extent of CSRO in this alloy system using diffraction techniques with sufficient sensitivity to resolve differences between rapidly solidified and thermally aged states. In the present work, we demonstrate the presence of CSRO via diffuse diffraction spots at the  $(1 \frac{1}{2} 0)$  position by combining neutron diffraction experiments with simulated diffraction patterns generated from atomistic configurations obtained using accurate machine-learning interatomic potentials [23]. These results provide direct experimental evidence that even the rapidly solidified state exhibits CSRO, albeit to a lesser degree than the thermally aged sample [24]. This indicates that the emergence of CSRO is directly linked to the attainment of lower free-energy configurations during the solidification process.

## 2. Experimental procedures

### 2.1 Alloy production

An equiatomic CrCoNi alloy was synthesized by inert gas atomization using argon (Ar), a process that ensures ultrafast solidification rates, employing commercially pure elements (99.9%). The resulting powders were sealed under an inert atmosphere in high-purity quartz tubes, annealed at 1373 K for 24 h, and subsequently water-quenched. Samples were investigated in the as-atomized state, after homogenization, and following various CSRO-aging treatments: 748 K for 100 h and 240 h, and 798 K for 24 h, also performed in encapsulated inert environments. All heat treatments were followed by water quenching. The sealing of the powders within quartz tubes prevented direct contact with water during the quenching process, ensuring that the samples were not exposed to oxidation or contamination. A summary of all experimental conditions analyzed in this study is provided in Table 1. The selection of thermal treatment temperatures and times were based on the work of Bacurau *et al.* [5], in which the presence of CSRO was indirectly detected.

Table 1: Nomenclature used throughout the text and thermal treatment conditions for each sample.

Name used in the text	Condition of treatment
Gas atomized	As-atomized
Homogenized	Annealed at 1373 K for 24 h + water quenching
100 h/748 K	Homogenized and aged at 748 K for 100 h
240 h/748 K	Homogenized and aged at 748 K for 240 h
24 h/798 K	Homogenized and aged at 798 K for 24 h

Microstructural characterization was performed using a scanning electron microscope (SEM, FEG Tecscan Mira3) equipped with energy-dispersive X-ray spectroscopy (EDS) and electron backscatter diffraction (EBSD) detectors, operating at an accelerating voltage of 25 kV. Sample preparation for microstructural analysis involved sequential grinding using SiC papers (220–1500 grit), followed by polishing with a 1  $\mu\text{m}$  alumina suspension. A final polishing step was performed for 12 h in a colloidal silica solution using a Buehler VibroMet 2 polisher.

These analyses were carried out to evaluate the crystallographic texture and compositional homogeneity of the sample aged for 240 h at 748 K. This condition was selected to assess the influence of thermal treatments on texture reduction in the alloy. From the EBSD measurements, both inverse pole figures (IPFs) and pole figures (PFs) were obtained. These representations use the unit m.r.d. (multiples of uniform random distribution), which indicates how many times the intensity of a given crystallographic orientation exceeds that of a completely random and uniform distribution [25], and guarantee that the measurements were performed on texture-free samples.

### 2.2 Neutron total scattering diffraction and Small-Angle Neutron Scattering analysis

Neutron total scattering and small-angle neutron scattering (SANS) experiments were performed on CrCoNi samples for all conditions listed in Table 1. All measurements were carried out at the Institut Laue-Langevin (ILL), Grenoble, France.

Total scattering data were collected on the D4 two-axis diffractometer. The incident beam size was  $12 \times 50$  mm<sup>2</sup>, and the wide-angle detector was scanned over an angular range from 1.3° to 140°, corresponding to a  $Q$ -range of 0.3–23.5  $\text{\AA}^{-1}$  at a wavelength of 0.499  $\text{\AA}$ , thereby providing access to high- $Q$  structural information. Two experimental configurations were employed. The first involved measurements of the empty sample holder, consisting of a cylindrical container made of pure vanadium with an outer diameter of approximately 8 mm. The second comprised measurements of the CrCoNi samples sealed in the same vanadium containers, ensuring experimental consistency and enabling accurate background subtraction.

SANS data were acquired at the ILL using the D16 diffractometer. The instrument configuration limited the maximum scattering vector to  $Q_{\text{max}} = 0.06 \text{\AA}^{-1}$ , thus probing structures larger than approximately 10 nm in real space. After background subtraction, the intensities were normalized by the illuminated area, incident flux, attenuator settings, and wavelength ( $\lambda = 4.5 \text{\AA}$ , take-off angle = 85°). As usual in SANS, the scattering vector  $Q$  is related to the real-space length scale through

$$d = \frac{2\pi}{Q},$$

where

$$Q = \frac{4\pi}{\lambda} \sin \theta.$$

### 2.3 Synchrotron X-ray diffraction

To compare the results obtained from neutron diffraction, three additional samples were produced under controlled thermal-processing conditions. Equiatomic CoCrNi alloys were synthesized by arc melting high-purity elements (all >99.99%) in an argon atmosphere. All three samples were extracted from the same ingot, with a total mass of approximately 50 g. The ingot was remelted five times to ensure chemical homogeneity, then homogenized at 1473 K for 4 h, followed by water quenching.

Subsequently, the material was hot-rolled at 1473 K to a thickness of 2 mm, cold-rolled to 50% reduction, and recrystallized by annealing at 1273 K for 1 h, again followed by water quenching. Finally, the rolled material was sectioned by electrical discharge machining (EDM) into specimens with dimensions of approximately 6 mm in length, 4 mm in width, and 1 mm in thickness for subsequent heat treatments.

After full recrystallization, two distinct aging treatments of 748 K for 100 h and 240 h were applied to promote different degrees of CSRO. In total, three samples were analyzed: the annealed state (1273 K / 1 h), and the two aged conditions (748 K / 100 h and 748 K / 240 h).

Synchrotron X-ray diffraction (SXRD) measurements were performed at the DESY P07 beamline using a wavelength of 0.142346 Å. A LaB standard was used to calibrate the sample-to-detector distance, detector tilt angle, and beam center. A Perkin-Elmer detector with a resolution of 2048 × 2048 pixels was employed for image acquisition, and the data were integrated using the PyFAI software [26] with 1024 points, converting the images into intensity versus  $2\theta$ .

### 2.4 Simulation Procedures

The simulated neutron diffraction patterns were obtained from independent Monte-Carlo (MC) modeling followed by molecular dynamics (MD) computations. Following an established methodology [27], equilibrium CSRO states were generated from independent atom-swap MC simulations on 4000-atom FCC supercells. These simulations were carried out using the Metropolis-Hasting algorithm [28], with Cr, Co, and Ni atoms initially distributed randomly on the FCC lattice. Each MC run was initialized with a lattice constant previously equilibrated via NPT-MD simulations using a Nosé-Hoover thermostat and barostat for 10,000 steps at the target temperature. During each MC simulation, 30 atom-swap attempts per atom (60,000 total) were performed to approach chemical equilibrium. This procedure was repeated for 300 K, 500 K, and 700 K to obtain equilibrium CSRO states at each temperature, while the initial configuration was used for the Random solid solution (RSS) state.

The final MC-equilibrated structures were then used as input for NPT-MD simulations. These simulations were performed at a constant temperature of 300 K, corresponding to room temperature of the diffraction measurements, and zero hydrostatic pressure for 5,000 steps with a 2.5 fs timestep. Forty independent simulations, each containing 4,000 atoms, were carried out for each CSRO state.

To mitigate finite-size effect in the atomistic simulations that could lead to a high signal-to-noise ratio in neutron diffraction analysis, supercells containing 32,000 atoms were constructed by combining 8 randomly selected snapshots from the 40 independent simulations of each CSRO state. The resulting supercells were then relaxed at fixed volume (i.e., energy minimized) before evaluating the neutron diffraction patterns. The relaxed supercells were then analyzed along the z-axis to evaluate the total projected intensity in this direction. Subsequently, a two-dimensional Fourier Transform (FT-2D) was applied to obtain diffraction patterns corresponding to the specific zone axes [110], [112], [111], and [100]. The analyses were performed under two distinct diffraction conditions: (*i*) X-ray diffraction (XRD), in which the atomic contrast was

weighted by the atomic numbers of each element, Cr (24), Co (27), and Ni (28); and (ii) neutron diffraction, using the neutron scattering lengths specific to each atom, Cr (3.64 fm), Co (2.49 fm), and Ni (10.3 fm).

All simulations were performed using LAMMPS (Large-scale Atomic/Molecular Massively Parallel Simulator) code [29], employing a Moment Tensor Potential [30] previously trained on high-fidelity ab-initio data specifically curated to capture CSRO effects and their impact on phase stability and related properties [23].

### 3. Results

#### 3.1 Microstructural results

Figure 1 presents the results obtained from SEM analysis. Figure 1a shows secondary electron (SE) and backscattered electron (BSE) images at different magnifications. These images indicate that, despite partial sintering induced by the thermal treatments, individual powder particles remain distinguishable and are not fully coalesced. Figure 1b displays the EDS maps, confirming the compositional homogeneity of the sample. Figures 1c present the inverse pole figure (IPF) map acquired via EBSD. The corresponding PFs are shown in Figures 1d. A weak crystallographic texture was observed, with maximum values below 1.5 m.r.d. These results indicate that the homogenization and aging treatments effectively minimized texture development in the material.

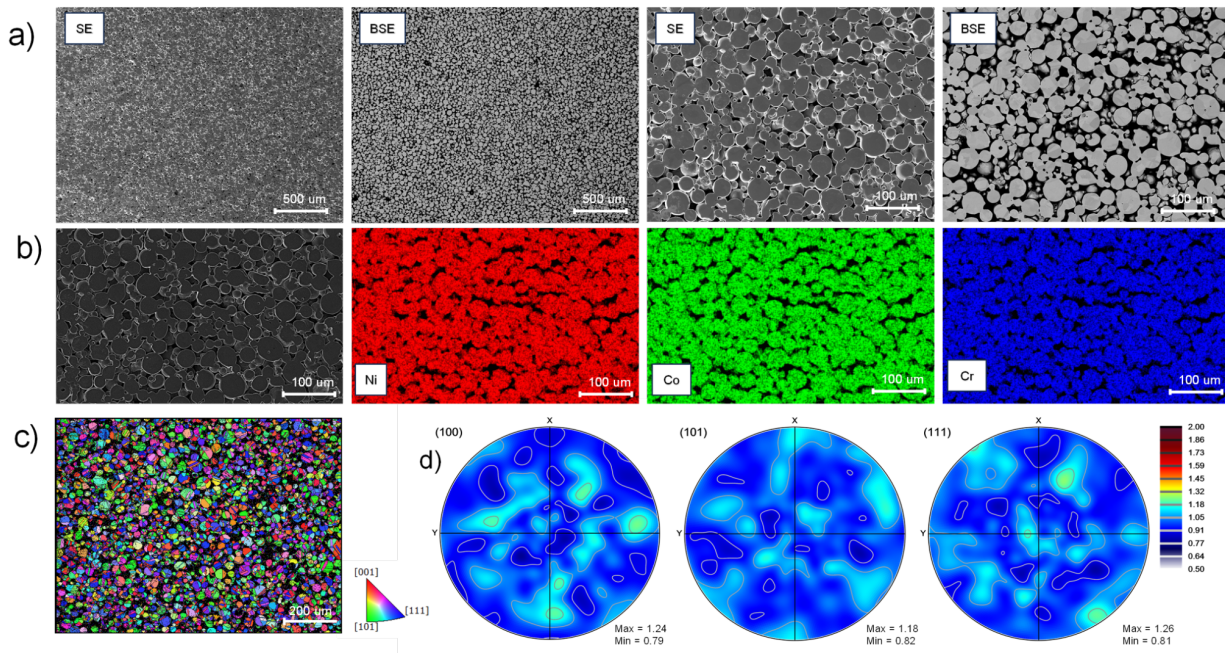


Fig. 1 – Scanning electron microscopy (SEM) analysis of the CoCrNi alloy aged for 240 h at 748 K. (a) Secondary electron (SE) and backscattered electron (BSE) images at different magnifications show that, despite the partial sintering caused by the thermal treatments, individual powder particles remain distinguishable and not fully coalesced. (b) Energy-dispersive X-ray spectroscopy (EDS) maps confirm the compositional homogeneity of the sample. (c) Inverse pole figure (IPF) map acquired via electron backscatter diffraction (EBSD). (d) Corresponding pole figures demonstrate that the applied processing successfully reduced crystallographic texture.

#### 3.2 Diffraction analysis results

Experimental neutron powder diffraction patterns are shown in Fig. 2. All patterns were normalized by their maximum intensity to allow direct comparison. The Bragg peaks are indistinguishable across all conditions, confirming that the samples remain fully single-phase FCC with no detectable changes in long-range crystallographic order. In contrast, a distinct diffuse peak is observed in the low- $Q$  region (highlighted by the red circle), centered near  $Q \approx 1.85 \text{ \AA}^{-1}$ .

The formation of CSRO is thermodynamically favored at lower temperatures, where the reduced influence

of entropy promotes local ordering [31]. However, because CSRO develops through a diffusional mechanism, its evolution at low temperatures requires longer aging times to reach equilibrium [5]. Figure 2b shows an expanded version of the region. For all samples, including the gas atomized sample, there appears to be some form of diffuse feature present. With subsequent heat treatment (either homogenization, or heat treatment), this diffuse feature appears to change. Whilst there is an apparent change between the three stages of sample preparation (gas-atomisation, homogenization, and subsequent heat treatment), there is little significant change in the observed between with the different post-homogenization heat treatments.

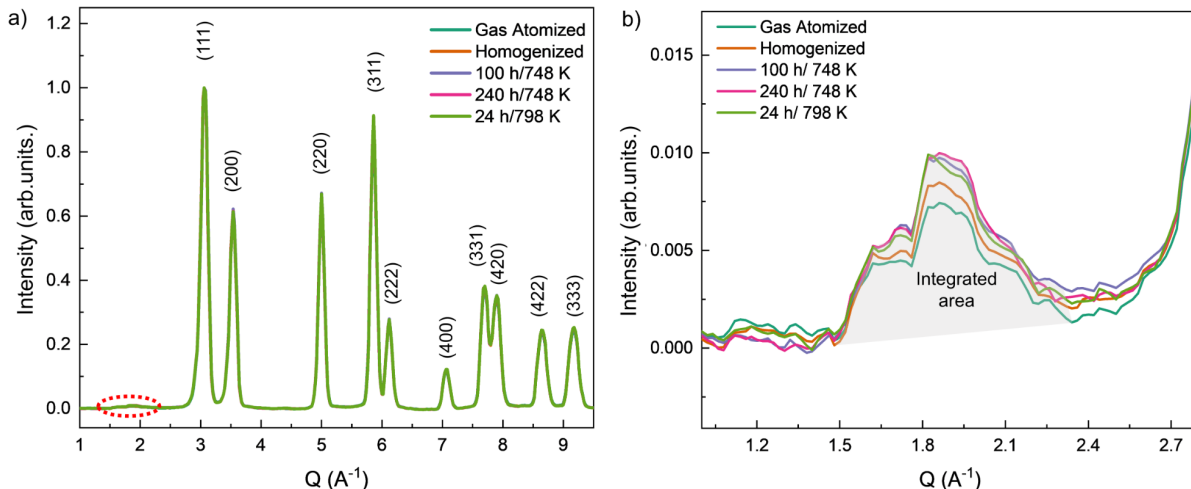


Fig. 2 – (a) Neutron powder diffraction patterns of CrCoNi under different processing conditions. All patterns were normalized to their respective maximum intensities. The Bragg peaks overlap perfectly for all states (as-atomized, homogenized, and aged), indicating identical average crystal structures and phase compositions. (b) The  $Q$  range between 1 and  $2.8 \text{ \AA}^{-1}$ , where the most pronounced diffuse scattering occurs. The diffuse peak reaches its maximum intensity at  $Q \approx 1.85 \text{ \AA}^{-1}$ , corresponding to the position of forbidden  $(1 \frac{1}{2} 0)$  reflections [22,32]. The gray-shaded region indicates the interval used to measure the CSRO level in each sample.

To measure this effect, the area under the diffuse scattering peaks was integrated over the same baseline (Fig. 2). The normalized areas for the three aged samples are the highest, and are essentially identical. This trend is consistent with calorimetric analyses [5], which indicate that CSRO saturation occurs after approximately 100 h of thermal treatment at 748 K for CrCoNi. For the sample aged for a shorter time at a higher temperature (24 h at 798 K), the observed behavior agrees with earlier results [33], which demonstrate through extensive electrical resistivity measurements that CSRO saturation is achieved in significantly shorter times when the temperature is increased to the 773–873 K range. Thus, it is reasonable to observe a comparable degree of CSRO in the 24 h/798 K condition to that obtained in the 240 h/748 K condition.

All results were normalized to the samples aged for 240 h at 748 K, which were taken as the reference corresponding to the maximum CSRO level achieved in this study. Remarkably, even the gas-atomized sample displays approximately 70% of the maximum diffuse intensity, indicating that local chemical ordering is not suppressed by rapid solidification [1,24]. This suggests that CSRO is a robust characteristic of the CrCoNi system: it forms almost instantaneously upon quenching; it persists across a wide range of processing routes; and it is further enhanced by low-temperature aging [1].

A similar trend was observed when analyzing the maximum intensity of the diffuse peak, with the same aging conditions (100 h and 240 h at 748 K, and 24 h at 798 K) exhibiting the highest values (Fig. 3). As with the area under the peaks, all aged samples display CSRO levels that are very close to each other, and within experimental uncertainty. This indicates that, although neutron diffraction is sufficiently sensitive to detect the presence of CSRO, it may not be able to resolve subtle differences in magnitude among closely related aging conditions.

Considering that previous studies [5], based on SXRD and TEM, have demonstrated that these heat-treatment conditions are insufficient to promote the formation of long-range ordered phases in equiatomic CoCrNi alloys, the present observations can be attributed to CSRO effects.

To further evaluate whether the CSRO-related diffuse scattering at low  $Q$  also affects the Bragg peaks associated with the FCC phase, both the maximum intensity and the integrated area of each reflection were analyzed (Supplementary Fig. 1a and 1b). These analyses revealed no significant differences among the samples subjected to different heat-treatment conditions, indicating that the FCC Bragg reflections remain unchanged. This confirms that the observed effect is intrinsically linked to the presence of CSRO, as the only detectable variation occurs in the low- $Q$  diffuse peak directly associated with the development of this phenomenon.

A previous study [34] employing high-energy X-ray diffraction on body-centered cubic (BCC) Fe-Ga alloys also reported the presence of CSRO. In this work CSRO was identified through diffuse peaks at low scattering angles, and the samples exhibiting the strongest diffuse intensity displayed behavior analogous to that observed in the present study.

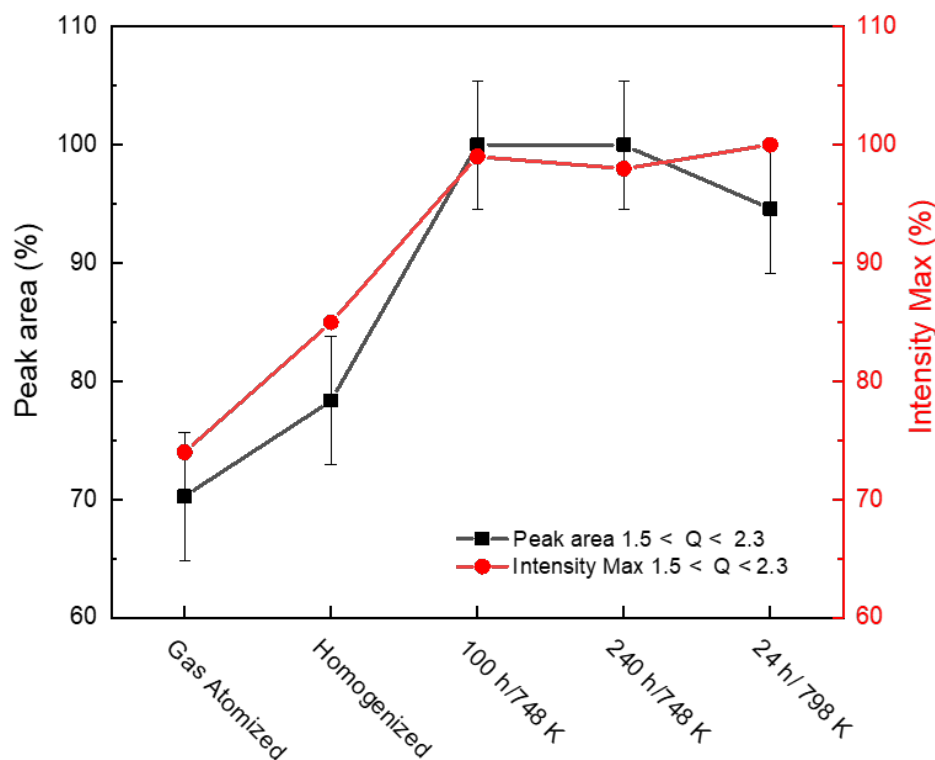


Fig. 3 – Measuring of CSRO in CrCoNi using the integrated area (black symbols) and maximum intensity (red symbols) of the diffuse scattering peak observed in neutron diffraction. The sample aged for 240 h at 748 K was taken as the reference condition and assigned 100% relative CSRO content, with all other states normalized accordingly. Remarkably, the as-atomized (gas-quenched) sample displays nearly 70% of the maximum CSRO, underscoring the speed with which local chemical correlations are established. The uncertainty in the area calculation was estimated from the quantified background noise, which was propagated to determine the error associated with the integrated diffuse peak area.

To further investigate the presence and evolution of CSRO in the CrCoNi alloy, we combined these neutron diffraction experiments with atomistic simulations. Four systems were modeled: one representing an RSS with no atomic ordering, and three additional configurations obtained by equilibrating the system at 700 K, 500 K, and 300 K to generate different levels of CSRO. All structures were fully relaxed, and their corresponding diffraction patterns were subsequently computed (Fig. 4). Consistent with earlier observations [29], the degree of CSRO increases systematically with decreasing equilibration temperature, with the 300

K configuration exhibiting the highest level of ordering and the 700 K configuration the lowest.

To ensure a meaningful comparison with neutron diffraction measurements acquired at room temperature, the MC-equilibrated structures associated with different CSRO states were subsequently relaxed via NPT molecular dynamics at 300 K and zero pressure. During this MD stage, atomic identities were kept fixed, no atom swaps were allowed, so that the CSRO levels obtained during MC equilibration were preserved. Although this procedure does not explicitly model rapid cooling, it provides a quenched configuration in which chemical correlations are frozen while lattice parameters and atomic vibrations equilibrate to the experimental measurement temperature. In this respect, the method mimics experimentally quenched samples: the degree of CSRO reflects the annealing temperature, whereas diffraction probes a room-temperature structure.

Computed neutron diffraction patterns (intensity vs  $Q$ , Section 2.4) and SXR D were compared directly with experimental measurements (Fig. 4). The simulations reproduce the primary neutron-diffraction features, including the diffuse peak between  $1.5 < Q < 2.4 \text{ \AA}^{-1}$  (blue circle) and the FCC Bragg reflections (Fig. 4a). Conversely, SXR D data show no indication of a diffuse peak at low  $Q$ . The weak features appearing at  $1.52 \text{ \AA}^{-1}$  and  $1.76 \text{ \AA}^{-1}$ , correspond to higher-order harmonics of the FCC reflections, resulting from the absence of a monochromator during the synchrotron experiment.

Figure 4b provides a magnified view of the  $1.2 < Q < 2.8 \text{ \AA}^{-1}$  range, where the diffuse scattering becomes more evident. Except for the RSS configuration (orange dash dot-dot line), all simulated structures exhibit a broad diffuse peak with maximum intensity near  $Q \approx 2.0 \text{ \AA}^{-1}$ , consistent with increased CSRO. The slight shift in the position of this feature between simulated and experimental patterns is attributed to differences in lattice parameters. As shown in Supplementary Fig. 2, the lattice parameters from the simulations are smaller than those measured experimentally, this is expected due to the overbending issue typical of PBE exchange–correlation functionals (used in the training of the machine learning potentials) [31]. Consequently, the smaller lattice spacing in the simulations results in diffraction features appearing at slightly higher  $Q$  values.

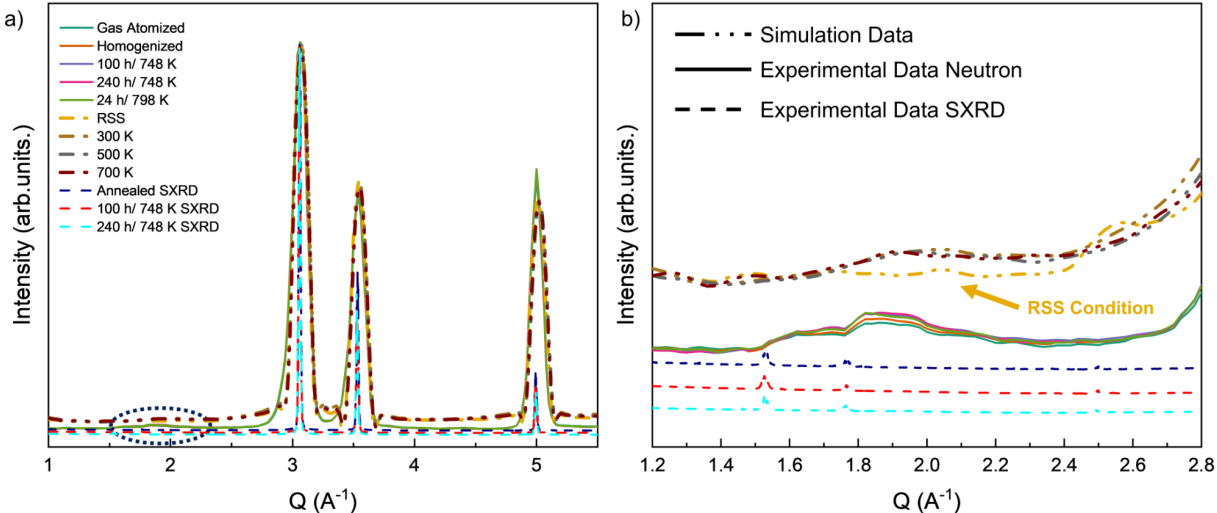


Fig. 4 – Comparison between experimental data and simulated neutron diffraction patterns. (a) The overlaid curves reveal the presence of a diffuse peak in the region  $1.4 < Q < 2.4 \text{ \AA}^{-1}$  (blue dotted circle), in addition to the Bragg peaks associated with the FCC phase. (b) A magnified view of the highlighted region confirms that the diffuse peak is reproduced in the simulated structures, demonstrating strong agreement between experimental observations and first-principles simulations. The SXR D data show no evidence of a diffuse peak, confirming that this technique lacks sufficient scattering contrast among Cr, Co, and Ni to resolve CSRO-related features. The simulated and SXR D curves were vertically offset for improved clarity.

Figures 5a, 5c, 5e, and 5g correspond to the real-space projection of the atomic structures along the z-axis,

yielding simulated atomic resolution images. These are analogous to high-resolution transmission electron microscopy (HRTEM) images but with neutron scattering contrasts instead, as the atomic contrast was weighted according to the neutron scattering lengths of Cr (3.64 fm), Co (2.49 fm), and Ni (10.3 fm), resulting in the contrast being dominated by Ni.

Although the visualization of arrays of atoms is difficult, Figures 5b, 5d, 5f, and 5h present the Fourier transforms of the atomic lattice images for each condition. These can be understood as a proxy for the single-crystal neutron diffraction pattern for each condition. Distinct features arise depending on the degree of CSRO. For the RSS and 700 K configurations, no significant diffuse scattering is detected between the main Bragg reflections (Figs. 5b and 5d). In contrast, as CSRO becomes more pronounced at lower temperatures, diffuse reflections emerge at half-integer positions, such as  $(1 \frac{1}{2} 0)$  along the  $[100]$  zone axis, highlighted by red circles in Figs. 4f and 4h. These features are most prominent in the 300 K configuration, consistent with the enhanced degree of chemical ordering.

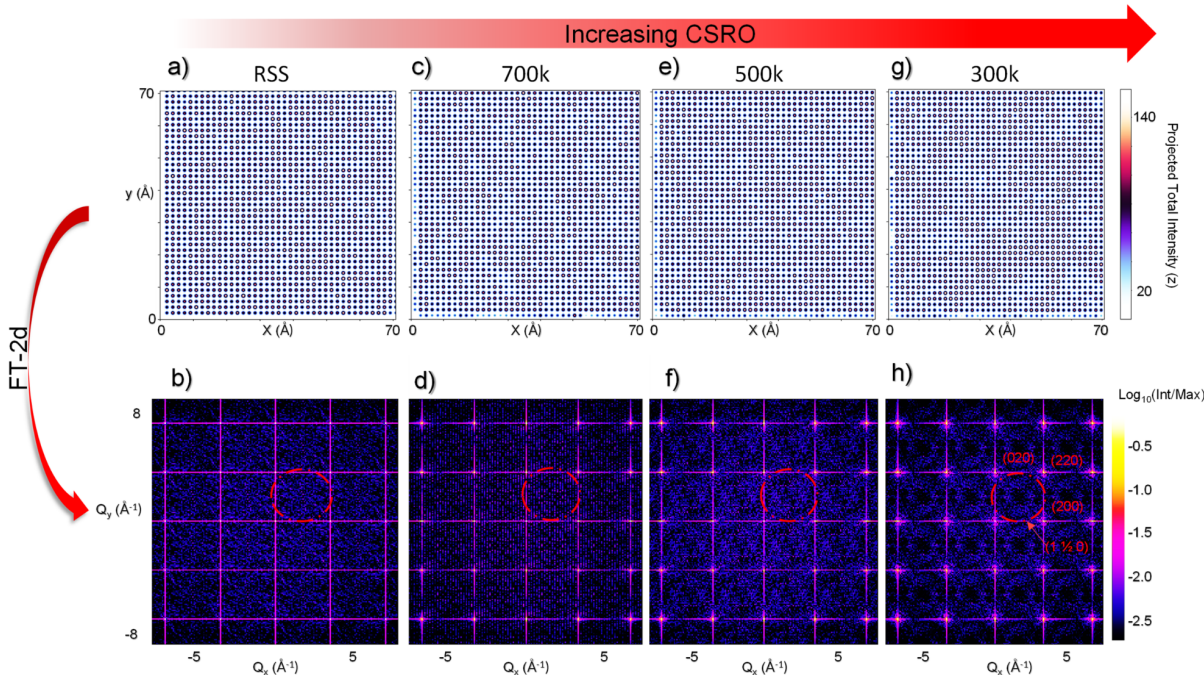


Fig. 5 – Simulations of atomic structures for different states. Panels (a) and (b) correspond to a random solid solution (no CSRO); (c) and (d) to a solid solution with CSRO annealed at 700 K; (e) and (f) to CSRO annealed at 500 K; and (g) and (h) to CSRO annealed at 300 K. The top images (a, c, e, g) show the real-space projection along the  $z$ -axis, while the bottom (b, d, f, h) displays the corresponding two-dimensional Fourier transforms (FT-2D), yielding the simulated neutron diffraction patterns along the  $[100]$  zone axis. Red circles highlight the diffuse spots associated with CSRO at the  $(1 \frac{1}{2} 0)$  position.

Based on the contrast observed in the FT-2D images, structural motifs resembling D1a ( $\text{Ni}_4\text{Mo}$  prototype),  $\text{Ni}_2\text{Cr}$ -type ordering ( $\text{Pt}_2\text{Mo}$  prototype), and  $\text{D0}_{22}$  ( $\text{Ni}_3\text{V}$  prototype) structures could be identified. These features have been previously reported in the literature through transmission electron microscopy as diffuse spots along the  $[100]$  zone axis at the  $(1 \frac{1}{2} 0)$  position, as well as in HRTEM images of compositions with sufficient chemical contrast [32,35,36]. However, in the present study, it was not possible to unambiguously determine which specific structural motif is primarily responsible for the observed diffuse spots. Notably, such features are absent along the other zone axes examined (Supplementary Fig. 4), further supporting their direct association with CSRO. In contrast, the presence of LRO would lead to well-defined superlattice reflections appearing along multiple zone axes, which is not observed in this case.

Notably, diffuse features are absent in the simulated X-ray diffraction patterns, which were generated using the atomic scattering factors of Cr (24), Co (27), and Ni (28) (Supplementary Fig. 5). This absence is

attributed to the low atomic number contrast among Cr, Co, and Ni for X-ray scattering. These results are consistent with the experimental SXR data (Fig. 4), which likewise failed to detect the diffuse peak, further confirming the limited sensitivity of X-rays (and thus electrons) to resolve CSRO related features in this alloy system. Moreover, along the [112] and [111] zone axis, no diffuse peaks were detected, in agreement with the findings reported by Coury et al. [16]. Their results indicate that the [112] orientation is not the most reliable direction for detecting CSRO, in contrast to several studies in the literature that have claimed CSRO signatures in CrCoNi-based alloys using electron diffraction along this zone axis [4,19,33,37]. Furthermore, the random supercell produces no observable diffuse intensity, reinforcing the interpretation that the half-order reflections are directly associated with CSRO.

The positions of the additional diffuse spots observed in the simulated patterns (Fig. 4f and 4h) are located around  $Q \approx 1.85 \text{ \AA}^{-1}$ , closely matching the diffuse peak identified in the experimental neutron diffraction data shown in Fig. 2b. This strong agreement supports the interpretation that the low- $Q$  diffuse scattering observed in the experimental samples arises from CSRO. The simulated patterns confirm that such features emerge in structures containing a high degree of CSRO, further corroborating the experimental observations.

### 3.2 Small-Angle Neutron Scattering analysis results

The anomaly observed in the high- $q$  SANS range, emerging near  $q \approx 1.2 \text{ \AA}^{-1}$  (corresponding to a real-space length scale of  $\sim 5.2 \text{ \AA}$ ), is consistently present across all aged CrCoNi samples. This feature is most likely an experimental artifact, as it coincides with the transition to a second detector configuration (lower intensity, increased statistical uncertainty). To mitigate its influence on the quantitative SANS analysis, the dataset was cropped to  $q < 1.125 \text{ \AA}^{-1}$ . Nevertheless, it is worth mentioning that this feature is sometimes documented in Ni-based alloys with CSRO or severe lattice distortions [14]. However, as shown in Supplementary Fig. 2, no substantial variations in the lattice parameter are observed among the samples, indicating that the applied heat treatments do not induce measurable lattice distortions.

In the low- $Q$  region, the scattering profile deviated from the classic Porod law ( $I \propto Q^{-4}$ ), exhibiting a power-law exponent between 1.9 and 2.5. According to the literature, an exponent of 2 is often encountered in disordered structures, such as polymers' strands coiled randomly; in the case of an ordered material, this exponent must be linked to randomly oriented flat objects scattering centers [38,39]. Current studies on steels have shown that an exponent near two is associated with precipitates with the form factor of an oblate spheroid or a thin disk [40]. The fine structure near  $Q \approx 0.2 \text{ \AA}^{-1}$  further suggests small compositional pockets or fluctuations (Figure 6a). To reconcile these premises and observations, we adopted a scattering model inspired in previous studies [41] combining (1) a Porod term (exponent fixed as 3) to represent the solid-solution, (2) a constant Laue background, (3) a lognormal distribution of randomly oriented disks to account for two-dimensional CSRO domains, and (4) an additional Lorentzian term to account for short-range compositional heterogeneities (Equation 1). The Lorentzian is scaled by the scattering length density contrast ( $\Delta\rho$ ) to obtain a more robust fit. Modeling and fit are performed with the aid of the jscatter library [42]. The complete fitting with residuals is provided as supplementary information Table S1.

$$I(Q) = Aq^{-3} + B + \Delta\rho^2 \cdot [vf_1 \cdot D(Q) + vf_2 \cdot S(Q)] \quad (1)$$

where:

- $A$  = Porod prefactor;
- $B$  = Laue background;
- $D(Q)$  Polydisperse disks: lognormal distribution with  $\sigma = 0.2$ , adjusted  $R$  (radius) and  $D$  (thickness);
- $S(Q) = I_0 / (1 + \xi^2 Q^2)$  (Lorentzian term with an adjustable correlation length  $\xi$ )
- $\Delta\rho = \text{SLD contrast} = 4.312 \times 10^{-4} \text{ nm}^2$ ,
- $vf_1, vf_2 = \text{volume frac. scaling factors}$

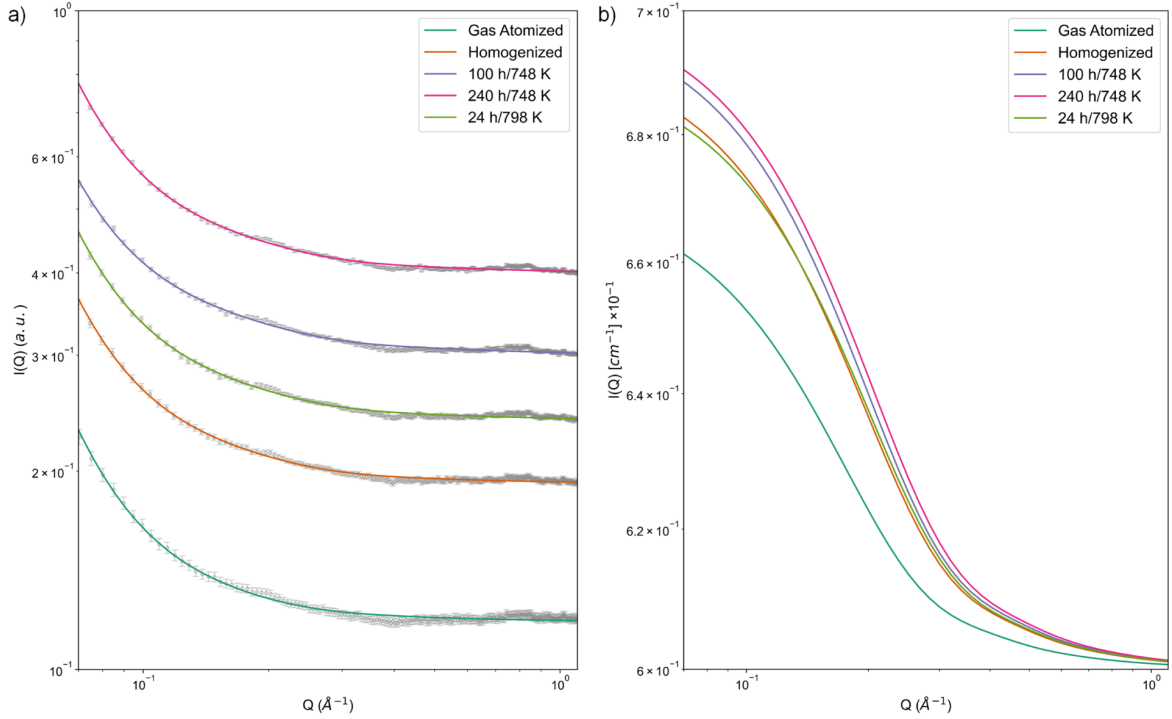


Figure 6 - (a) SANS data from equiatomic CoCrNi samples subjected to different processing and thermal treatments; the markers with error bars (gray) indicate experimental data while the solid lines (colored) represent the fitted models. (b) isolated contribution of SRO disks + Lorentzian for scattering in each sample; the flat background was fixed to 0.6. in the images, intensities are multiplied by  $10^6$  for visualization purposes.

The neutron scattering length density (SLD) contrast was calculated assuming four atoms per FCC unit cell with lattice parameter  $a = 3.564 \times 10^{-8}$  cm. The ordered phase was considered pure Ni, with a scattering length  $b = 1.03 \times 10^{-12}$  cm. The solid solution was assigned the average contrast of Ni, Co ( $b = 0.249 \times 10^{-12}$  cm), and Cr ( $b = 0.3635 \times 10^{-12}$  cm) [43].

The fitting procedure yielded consistent geometric parameters for the disk-like features, with radii of  $\sim 11$  Å and thicknesses of  $\sim 1$  Å ( $\sigma = 0.2$ ). The volumetric fraction of these disks, quantified as CSRO domains, exhibits significant thermal activation. Relative to the gas atomized powder (minimal  $vf_1 = 5.343 \times 10^{-6}$ ), aging at 798 K for 24 h induced a 2.25-fold increase in CSRO cluster density, while prolonged aging at 748 K (240 h) further enhanced it to 2.63 times relative to the reference. These clusters are at least one order of magnitude smaller than second-phase precipitates usually analyzed via SANS [40], but larger than the radius of gyration  $R_g \sim 3$  Å proposed by Hsiao et al. [14] under similar conditions. This parameter describes the average size and spatial distribution of atomic density within a cluster, providing a quantitative measure of its nanoscale extent. The volume of CSRO based on the scaling factor of disks ( $vf_1$ ) is as follows: aging at 748 K (240 h > 100 h) > aging at 798 K (24 h) > Homogenized > Gas atomized. The volume fraction of disk-shaped features ( $vf_1$ ) and other best-fit parameters, along with their associated uncertainties, are provided in Supplementary Table S1. It is worth noting that, even in the absence of precipitate formation in the samples, the SANS profiles differ significantly from one another, indicating variations in the atomic arrangement.

The Lorentzian term improves the fitting stability, but the correlation length ( $\xi$ ) is saturated at the minimum (bound) of 1.0 Å, which is comparable to the atomic radius of Ni ( $\sim 1.24$  Å), thus too small to associate with CSRO. At the same time, the  $vf_2$  scaling factor follows the same trend as  $vf_1$ . Relative to the homogenized reference sample (minimal  $vf_2 = 3.56$  %),  $vf_2$  increases by a factor of 1.33 in the sample aged at 798 K and by 2.03 in the sample aged at 748 K (100 h). Such a behavior is highlighted in Fig. 6b. It is worth mentioning

that despite  $vf_2$  being  $10^4$  larger than  $vf_1$ , the disks dominate scattering due to their form factor scaling as  $(\pi R^2 D)^2$  (i.e.,  $R^4 D^2$ ), with  $R$  and  $D$  being the radius and the thickness of disks, while the Lorentzian term scales weakly with  $\xi^3$ .

## 4. Discussion

### 4.1 Origin of Diffuse Spots Along the [100] Zone Axis at the $(1 \frac{1}{2} 0)$ Position

CSRO in metallic alloys typically manifests as broad and diffuse intensity maxima in reciprocal space [32]. These maxima occur at points where the second derivative of the free energy reaches a minimum, locations that, for symmetry reasons, satisfy the Lifshitz criterion, which requires that two or more symmetry elements intersect at the same position in reciprocal space [44]. The main distinction between CSRO and LRO lies in the nature of the additional reflections. In LRO, well-defined superlattice peaks appear at multiple reciprocal-space positions and across different zone axes, reflecting the periodicity of the ordered phase. In contrast, in the present work, CSRO is characterized by the presence of diffuse reflections, typically located at positions of the type  $(1 \frac{1}{2} 0)$  along the [100] zone axis in FCC structures. These features arise from local atomic ordering associated with the  $\{420\}$  family of planes [32,36].

The occurrence of diffuse spots at  $(1 \frac{1}{2} 0)$ , observed along the [100] zone axis, has been widely reported in alloys with an FCC structure and is invariably attributed to the presence of CSRO. Van Tendeloo and Amelinckx [32] investigated  $Ni_4Mo$ ,  $Au_4Cr$ ,  $Au_4V$ , and  $Au_4Fe$  alloys using HRTEM after heat treatments carefully designed to suppress the formation of long-range ordered phases. In these systems, the chemical contrast between constituent elements is sufficient to enable the detection of CSRO via transmission electron microscopy, which is not the case for the CrCoNi alloy. In all instances, diffuse reflections at  $(1 \frac{1}{2} 0)$  were identified prior to second phase precipitation, although with varying intensities, more pronounced in  $Ni_4Mo$  and weaker in  $Au_4Fe$ . The authors interpreted these reflections as structural projections associated with the  $D1_a$  and  $D0_{22}$  phases.

Similar results were later reported by Hata et al. [36] in the Ni–19.5% Mo alloy, also analyzed by HRTEM. Using Fourier transformation with a doughnut-shaped aperture, the authors confirmed the presence of diffuse spots at  $(1 \frac{1}{2} 0)$  along the [100] axis. After background noise reduction in the HRTEM images, patterns consistent with the structural projections  $D1_a$ ,  $D0_{22}$ ,  $Pt_2Mo$ , and  $N_2M_2$  were identified, the latter being embedded in the FCC matrix. The observation of  $N_2M_2$  patterns was consistent with the maximum intensities detected at  $(1 \frac{1}{2} 0)$ , while mixed configurations of  $D1_a$ ,  $D0_{22}$ , and  $Pt_2Mo$  were also reported in other studies [35,45,46], indicating that at least part of these projections contributes to the origin of the diffuse reflections. In the same work, the experimental results were corroborated by Monte Carlo simulations, which reproduced similar diffuse patterns, further reinforcing the connection between the  $(1 \frac{1}{2} 0)$  reflections and the presence of CSRO.

In the present work, and in comparison with the studies mentioned above, the FT-2D patterns derived from the simulated structures also revealed diffuse reflections at the  $(1 \frac{1}{2} 0)$  position, consistent with the projection of the  $D1_a$  structure observed in simulated FFT patterns [32]. It is worth noting that the simulated neutron-based images were generated from monocrystalline models, which may contribute to the reduced visibility of other possible structural motifs, such as  $D0_{22}$  and  $Pt_2Mo$ , as reported in previous studies. Based on these simulated structures, the manifestation of CSRO in equiatomic CrCoNi can be associated with reflections arising from projections related to  $D1_a$ -,  $Pt_2Mo$ -, and  $D0_{22}$ -type motifs. However, it is not possible to unambiguously identify the dominant configuration, and further experimental investigations on single-crystal samples are required to reach a definitive conclusion. Furthermore, only minimal contrast is expected in electron and X-ray diffraction patterns along the [100] zone axis for CrCoNi, due to the very similar structure factors of Cr, Co, and Ni. This explains why such diffuse features have not been observed using these techniques (as shown in Supplementary Figs. 5 and 6).

### 4.2 SANS discussion

The SANS models proposed in this work align well with recent atom probe tomography (APT) data published by Li et al. [47]. Their study identified excess Ni-Ni bonds within clusters ranging from 20 to 155 atoms (equivalent to diameters of 0.7–1.5 nm), consistent with our disk sizes (2.2 nm diameter). Furthermore, while the authors mention in the main text that most (number density) CSRO domains are spherical, their

supplementary data reveal occasional 2D Ni-Ni clusters (disks or rods) that typically contain up to 300 atoms. Given that scattered intensity scales with the square of the volume, even a small population of such bidimensional clusters would dominate the SANS signal, as proposed herein. It is important to note that the scattering length of Ni is significantly different from Co and Cr, which are similar to one another, thus, the neutron diffraction data will display enhanced contrast when Ni-based features are present. Thus, there might be other types and shapes of CSRO-related domains in this alloy but these are the most prominent regarding Ni.

## 5. Conclusions

Neutron diffraction results revealed variations in diffuse intensity scattering near  $Q \approx 1.85 \text{ \AA}^{-1}$ . Simulated structures generated by MD/MC methods reproduced diffuse scattering at low angles, analogous to the experimental observations, suggesting CSRO as the origin of these signals.

Based on these results, the extent of CSRO was measured by integrating the area under the diffuse scattering peak. Samples aged at 748 K for 100 h and 240 h, as well as the sample aged at the slightly higher temperature of 798 K for 24 h, exhibited a significantly higher degree of CSRO compared to the as-atomized and homogenized conditions. Remarkably, even the rapidly solidified powder displayed approximately 70% of the CSRO level observed in the sample aged for 240 h, indicating that this ordering phenomenon is quick enough to stabilize the phase even during rapid solidification.

Analysis of the simulated structures through *FT-2D* revealed the presence of diffuse reflections along the [100] zone axis at the  $(1 \frac{1}{2} 0)$  positions, features commonly reported in other FCC alloys exhibiting CSRO. These reflections can be associated with structural motifs such as D1a, Pt<sub>2</sub>Mo, and D0<sub>22</sub>, as described in the literature.

The SANS results indicate that the contribution of Ni-rich domains (disks or rods) to neutron scattering cannot be neglected. The disk form factor implies that CSRO manifests as localized, plate-like compositional fluctuations rather than isotropic clusters, aligning with observations from atom-probe tomography.

Neutron diffraction is a powerful technique for detecting CSRO in CrCoNi, overcoming the limitations of transmission electron diffraction, where the low contrast among Cr, Co, and Ni hinders direct observation of the phenomenon. As such, the neutron-based approach establishes a robust and sensitive pathway for identifying and measuring CSRO in this system.

**Acknowledgment:** V.P.B. was supported by Fundação de Amparo à Pesquisa do Estado de São Paulo - Brasil (FAPESP) under grants 2024/02515-2 To CAPES - Coordenação de Aperfeiçoamento de Pessoal de Nível Superior for their financial support in this work through a scholarship, process no. 88887.952714/2024-00. This study was financed in part by the Coordenação de Aperfeiçoamento de Pessoal de Nível Superior - Brasil (CAPES) - Finance Code 001. G.C.S. was supported by Fundação de Amparo à Pesquisa do Estado de São Paulo - Brasil (FAPESP) under grant 2023/07403-5. A.F.A. acknowledges the financial support from FAPESP, grant 2024/11008-7 and the National Council for Scientific and Technological Development [CNPQ, grants 157806/2025-1 and 153727/2024-1]. E.M.M. acknowledges Conselho Nacional de Desenvolvimento Científico e Tecnológico (CNPq) processes 444505/2024-5 and 403997/2025-9. F.G.C. acknowledges the Fundação de Amparo à Pesquisa do Estado de São Paulo (FAPESP), process number 2022/02770-7, and the Conselho Nacional de Desenvolvimento Científico e Tecnológico (CNPq), processes 403832/2023-3 and 444393/2024-2, for the financial support. The research was sponsored by the Army Research Office and was accomplished under Grant Number W911NF-23-1-0310. The views and conclusions contained in this document are those of the authors and should not be interpreted as representing the official policies, either expressed or implied, of the Army Research Office or the U.S. Government. The U.S. Government is authorized to reproduce and distribute reprints for Government purposes notwithstanding any copyright notation herein. The authors thank the Laboratory of Structural Characterization (LCE/ DEMa/UFSCar) for the general facilities. We acknowledge DESY (Hamburg, Germany), a member of the Helmholtz Association HGF, for the provision of experimental facilities. Parts of this research were carried out at PETRA III and we would like to thank Drs. Norbert Schell, Emad Maawad, and Martin Etter for assistance in using the P07 beamline. The authors would like to sincerely acknowledge the Institut Laue-Langevin (ILL), Grenoble, France, for providing the neutron beamtime and experimental facilities. We are especially grateful to Dr.

Gabriel Julio Cuello for his valuable support and assistance during the experiments performed on the D4 instrument, as well as to Dr. Viviana Cristiglio for her essential help during the experiments carried out on the D16 instrument. Their expertise and guidance were fundamental to the successful completion of this work.

**Author contributions:** CRediT V.P.B., F.G.C., and E.M.M. conceptualized this research and designed the entire workflow. V.P.B. and G.C.S. conducted all the production and processing of the alloys used in the study. V.P.B., C.B.S., C.S., and L.O. conducted the neutron total scattering diffraction and small-angle neutron scattering analyses. F.G.C. conducted synchrotron radiation diffraction. R.F. and Y.C. conducted the MD-MC analyses. V.P.B., G.C.S., and F.G.C. processed data obtained from neutron total scattering diffraction. C.S. processed data obtained from small-angle neutron scattering analyses. V.P.B., F.G.C., and E.M.M. drafted the first manuscript. A.F.A., L.O. and D.M. revised the manuscript.

**Declaration of Competing Interests:** The authors declare that they have no known competing financial interests or personal relationships that could have appeared to influence the work reported in this paper.

**Data and materials availability:** The data supporting the findings in this study are available within the paper. Any further information or clarification is available from the corresponding author upon reasonable request.

## References

- [1] Y. Han, H. Chen, Y. Sun, J. Liu, S. Wei, B. Xie, Z. Zhang, Y. Zhu, M. Li, J. Yang, W. Chen, P. Cao, Y. Yang, Ubiquitous short-range order in multi-principal element alloys, *Nat. Commun.* 15 (2024) 6486. <https://doi.org/10.1038/s41467-024-49606-1>.
- [2] W.H. Blades, B.W.Y. Redemann, N. Smith, D. Sur, M.S. Barbieri, Y. Xie, S. Lech, E. Anber, M.L. Taheri, C. Wolverton, T.M. McQueen, J.R. Scully, K. Sieradzki, Tuning chemical short-range order for stainless behavior at reduced chromium concentrations in multi-principal element alloys, *Acta Mater.* 277 (2024) 120209. <https://doi.org/10.1016/j.actamat.2024.120209>.
- [3] X. Chen, Q. Wang, Z. Cheng, M. Zhu, H. Zhou, P. Jiang, L. Zhou, Q. Xue, F. Yuan, J. Zhu, X. Wu, E. Ma, Direct observation of chemical short-range order in a medium-entropy alloy, *Nature.* 592 (2021) 712–716. <https://doi.org/10.1038/s41586-021-03428-z>.
- [4] L. Zhou, Q. Wang, J. Wang, X. Chen, P. Jiang, H. Zhou, F. Yuan, X. Wu, Z. Cheng, E. Ma, Atomic-scale evidence of chemical short-range order in CrCoNi medium-entropy alloy, *Acta Mater.* 224 (2022) 117490. <https://doi.org/10.1016/j.actamat.2021.117490>.
- [5] V.P. Bacurau, P.A.F.P. Moreira, G. Bertoli, A.F. Andreoli, E. Mazzer, F.F. de Assis, P. Gargarella, G. Koga, G.C. Stumpf, S.J.A. Figueroa, M. Widom, M. Kaufman, A. Fantin, Y. Cao, R. Freitas, D. Miracle, F.G. Coury, Comprehensive analysis of ordering in CoCrNi and CrNi2 alloys, *Nat. Commun.* 15 (2024) 7815. <https://doi.org/10.1038/s41467-024-52018-w>.
- [6] E.P. George, D. Raabe, R.O. Ritchie, High-entropy alloys, *Nat. Rev. Mater.* 4 (2019) 515–534. <https://doi.org/10.1038/s41578-019-0121-4>.
- [7] Y. Zhang, T.T. Zuo, Z. Tang, M.C. Gao, K.A. Dahmen, P.K. Liaw, Z.P. Lu, Microstructures and properties of high-entropy alloys, *Prog. Mater. Sci.* 61 (2014) 1–93. <https://doi.org/10.1016/j.pmatsci.2013.10.001>.
- [8] B. Gludovatz, A. Hohenwarter, K.V.S. Thurston, H. Bei, Z. Wu, E.P. George, R.O. Ritchie, Exceptional damage-tolerance of a medium-entropy alloy CrCoNi at cryogenic temperatures, *Nat. Commun.* 7 (2016) 10602. <https://doi.org/10.1038/ncomms10602>.
- [9] B. Gwalani, T. Alam, C. Miller, T. Rojhirunsakool, Y.S. Kim, S.S. Kim, M.J. Kaufman, Y. Ren, R. Banerjee, Experimental investigation of the ordering pathway in a Ni-33 at.%Cr alloy, *Acta Mater.* 115 (2016) 372–384. <https://doi.org/10.1016/j.actamat.2016.06.014>.
- [10] S.M. Dubiel, J. Cieslak, Short-range order in iron-rich Fe-Cr alloys as revealed by Mössbauer spectroscopy, *Phys. Rev. B.* 83 (2011) 180202. <https://doi.org/10.1103/PhysRevB.83.180202>.

- [11] B. Stephan, D. Jacob, F. Delabrouille, L. Legras, A kinetic study of order-disorder transition in ni-cr based alloys, *Miner. Met. Mater. Ser.* (2019) 233–249. [https://doi.org/10.1007/978-3-030-04639-2\\_15](https://doi.org/10.1007/978-3-030-04639-2_15).
- [12] Y. Liu, H. Lou, F. Zhang, Z. Zeng, Q. Zeng, Short-range order in binary and multiple principal element alloys: A review, *Matter Radiat. Extrem.* 10 (2025). <https://doi.org/10.1063/5.0275123>.
- [13] F.X. Zhang, S. Zhao, K. Jin, H. Xue, G. Velisa, H. Bei, R. Huang, J.Y.P. Ko, D.C. Pagan, J.C. Neufeind, W.J. Weber, Y. Zhang, Local Structure and Short-Range Order in a NiCoCr Solid Solution Alloy, *Phys. Rev. Lett.* 118 (2017) 205501. <https://doi.org/10.1103/PhysRevLett.118.205501>.
- [14] H.-W. Hsiao, R. Feng, H. Ni, K. An, J.D. Poplawsky, P.K. Liaw, J.-M. Zuo, Data-driven electron-diffraction approach reveals local short-range ordering in CrCoNi with ordering effects, *Nat. Commun.* 13 (2022) 6651. <https://doi.org/10.1038/s41467-022-34335-0>.
- [15] H. Jores, B. Ravel, E. Anber, J. Hollenbach, D. Sur, J. Hattrick-Simpers, M.L. Taheri, B. DeCost, Why is EXAFS for complex concentrated alloys so hard? Challenges and opportunities for measuring ordering with X-ray absorption spectroscopy, *Matter.* 6 (2023) 3763–3781. <https://doi.org/10.1016/j.matt.2023.09.010>.
- [16] F.G. Coury, C. Miller, R. Field, M. Kaufman, On the origin of diffuse intensities in fcc electron diffraction patterns, *Nature.* 622 (2023) 742–747. <https://doi.org/10.1038/s41586-023-06530-6>.
- [17] F. Walsh, M. Zhang, R.O. Ritchie, M. Asta, A.M. Minor, Multiple origins of extra electron diffractions in fcc metals, *Sci. Adv.* 10 (2024). <https://doi.org/10.1126/sciadv.adn9673>.
- [18] L.R. Owen, H.Y. Playford, H.J. Stone, M.G. Tucker, A new approach to the analysis of short-range order in alloys using total scattering, *Acta Mater.* 115 (2016) 155–166. <https://doi.org/10.1016/j.actamat.2016.05.031>.
- [19] R. Zhang, S. Zhao, J. Ding, Y. Chong, T. Jia, C. Ophus, M. Asta, R.O. Ritchie, A.M. Minor, Short-range order and its impact on the CrCoNi medium-entropy alloy, *Nature.* 581 (2020) 283–287. <https://doi.org/10.1038/s41586-020-2275-z>.
- [20] A.F. Andreoli, A. Fantin, S. Kasatkov, V.P. Bacurau, M. Widom, P. Gargarella, E.M. Mazzer, T.G. Woodcock, K. Nielsch, F.G. Coury, The impact of chemical short-range order on the thermophysical properties of medium- and high-entropy alloys, *Mater. Des.* 238 (2024) 112724. <https://doi.org/10.1016/j.matdes.2024.112724>.
- [21] F. Walsh, M. Asta, R.O. Ritchie, Magnetically driven short-range order can explain anomalous measurements in CrCoNi, *Proc. Natl. Acad. Sci. U. S. A.* 118 (2021) 1–6. <https://doi.org/10.1073/pnas.2020540118>.
- [22] W. Schweika, H.G. Haubold, Neutron-scattering and Monte Carlo study of short-range order and atomic interaction in Ni<sub>0.89</sub>Cr<sub>0.11</sub>, *Phys. Rev. B.* 37 (1988) 9240–9248. <https://doi.org/10.1103/PhysRevB.37.9240>.
- [23] Y. Cao, K. Sheriff, R. Freitas, Capturing short-range order in high-entropy alloys with machine learning potentials, (2024) 40–42. <http://arxiv.org/abs/2401.06622>.
- [24] M. Islam, K. Sheriff, Y. Cao, R. Freitas, Nonequilibrium chemical short-range order in metallic alloys, *Nat. Commun.* 16 (2025) 8926. <https://doi.org/10.1038/s41467-025-64733-z>.
- [25] A.I. Saville, S.C. Vogel, A. Creuziger, J.T. Benzing, A.L. Pilchak, P. Nandwana, J. Klemm-Toole, K.D. Clarke, S.L. Semiatin, A.J. Clarke, Texture evolution as a function of scan strategy and build height in electron beam melted Ti-6Al-4V, *Addit. Manuf.* 46 (2021) 102118. <https://doi.org/10.1016/j.addma.2021.102118>.
- [26] J. Kieffer, D. Karkoulis, PyFAI, a versatile library for azimuthal regrouping, *J. Phys. Conf. Ser.* 425 (2013) 202012. <https://doi.org/10.1088/1742-6596/425/20/202012>.
- [27] K. Sheriff, Y. Cao, T. Smidt, R. Freitas, Quantifying chemical short-range order in metallic alloys, *Proc. Natl. Acad. Sci.* 121 (2024). <https://doi.org/10.1073/pnas.2322962121>.
- [28] N. Metropolis, A.W. Rosenbluth, M.N. Rosenbluth, A.H. Teller, E. Teller, Equation of State Calculations by Fast Computing Machines, *J. Chem. Phys.* 21 (1953) 1087–1092. <https://doi.org/10.1063/1.1699114>.
- [29] S. Plimpton, Fast Parallel Algorithms for Short-Range Molecular Dynamics, *J. Comput. Phys.* 117 (1995) 1–19. <https://doi.org/10.1006/jcph.1995.1039>.

- [30] A. V. Shapeev, Moment Tensor Potentials: A Class of Systematically Improvable Interatomic Potentials, *Multiscale Model. Simul.* 14 (2016) 1153–1173. <https://doi.org/10.1137/15M1054183>.
- [31] F. Coury, G. Stumpf, Y. Cao, V. Bacurau, D. Miracle, W. Wolf, E. Zanotto, R. Freitas, On the nature of chemical short-range order evolution, (2025). <https://www.researchsquare.com/article/rs-7339299/v1>.
- [32] G. Van Tendeloo, S. Amelinckx, D. de Fontaine, On the nature of the “short-range order” in 1 1/2 0 alloys, *Acta Crystallogr. Sect. B Struct. Sci.* 41 (1985) 281–292. <https://doi.org/10.1107/S0108768185002166>.
- [33] L. Li, Z. Chen, S. Kuroiwa, M. Ito, K. Yuge, K. Kishida, H. Tanimoto, Y. Yu, H. Inui, E.P. George, Evolution of short-range order and its effects on the plastic deformation behavior of single crystals of the equiatomic Cr-Co-Ni medium-entropy alloy, *Acta Mater.* 243 (2023) 118537. <https://doi.org/10.1016/j.actamat.2022.118537>.
- [34] S. Guruswamy, T. V. Jayaraman, R.P. Corson, G. Garside, S. Thuanboon, Short range ordering and magnetostriction in Fe-Ga and other Fe alloy single crystals, *J. Appl. Phys.* 104 (2008). <https://doi.org/10.1063/1.3040154>.
- [35] K.H. Lee, K. Hiraga, D. Shindo, M. Hirabayashi, High resolution electron microscopic study of the ordering processes in Ni<sub>4</sub>Mo alloy, *Acta Metall.* 36 (1988) 641–649. [https://doi.org/10.1016/0001-6160\(88\)90098-3](https://doi.org/10.1016/0001-6160(88)90098-3).
- [36] S. Hata, S. Matsumura, N. Kuwano, K. Oki, D. Shindo, Short range order in Ni<sub>4</sub>Mo and its high resolution electron microscope images, *Acta Mater.* 46 (1998) 4955–4961. [https://doi.org/10.1016/S1359-6454\(98\)00180-3](https://doi.org/10.1016/S1359-6454(98)00180-3).
- [37] M. Zhang, Q. Yu, C. Frey, F. Walsh, M.I. Payne, P. Kumar, D. Liu, T.M. Pollock, M.D. Asta, R.O. Ritchie, A.M. Minor, Determination of peak ordering in the CrCoNi medium-entropy alloy via nanoindentation, *Acta Mater.* 241 (2022) 118380. <https://doi.org/10.1016/j.actamat.2022.118380>.
- [38] C.J. Gommers, S. Jaksch, H. Frielinghaus, Small-angle scattering for beginners, *J. Appl. Crystallogr.* 54 (2021) 1832–1843. <https://doi.org/10.1107/S1600576721010293>.
- [39] J. Eyssautier, P. Levitz, D. Espinat, J. Jestin, J. Gummel, I. Grillo, L. Barré, Insight into Asphaltene Nanoaggregate Structure Inferred by Small Angle Neutron and X-ray Scattering, *J. Phys. Chem. B.* 115 (2011) 6827–6837. <https://doi.org/10.1021/jp111468d>.
- [40] Y.Q. Wang, S.J. Clark, V. Janik, R.K. Heenan, D.A. Venero, K. Yan, D.G. McCartney, S. Sridhar, P.D. Lee, Investigating nano-precipitation in a V-containing HSLA steel using small angle neutron scattering, *Acta Mater.* 145 (2018) 84–96. <https://doi.org/10.1016/j.actamat.2017.11.032>.
- [41] G. Spartacus, J. Malaplate, F. De Geuser, I. Mouton, D. Sornin, M. Perez, R. Guillou, B. Arnal, E. Rouesne, A. Deschamps, Chemical and structural evolution of nano-oxides from mechanical alloying to consolidated ferritic oxide dispersion strengthened steel, *Acta Mater.* 233 (2022) 117992. <https://doi.org/10.1016/j.actamat.2022.117992>.
- [42] R. Biehl, Jscatter, a program for evaluation and analysis of experimental data, *PLoS One.* 14 (2019) e0218789. <https://doi.org/10.1371/journal.pone.0218789>.
- [43] V.F. Sears, Neutron scattering lengths and cross sections, *Neutron News.* 3 (1992) 26–37. <https://doi.org/10.1080/10448639208218770>.
- [44] D. De Fontaine, Configurational Thermodynamics of Solid Solutions, in: 1979: pp. 73–274. [https://doi.org/10.1016/S0081-1947\(08\)60360-4](https://doi.org/10.1016/S0081-1947(08)60360-4).
- [45] P. De Meulenaere, G. Van Tendeloo, J. Van Landuyt, D. Van Dyck, On the interpretation of HREM images of partially ordered alloys, *Ultramicroscopy.* 60 (1995) 265–282. [https://doi.org/10.1016/0304-3991\(95\)00065-9](https://doi.org/10.1016/0304-3991(95)00065-9).
- [46] A. Verma, N. Wanderka, J.B. Singh, M. Sundararaman, J. Banhart, On the evolution of long-range order from short-range order in a Ni<sub>2</sub>(Cr<sub>0.5</sub>Mo<sub>0.5</sub>) alloy, *J. Alloys Compd.* 586 (2014) 561–566. <https://doi.org/10.1016/j.jallcom.2013.10.086>.

[47] Y. Li, T. Colnaghi, Y. Gong, H. Zhang, Y. Yu, Y. Wei, B. Gan, M. Song, A. Marek, M. Rampp, S. Zhang, Z. Pei, M. Wuttig, S. Ghosh, F. Körmann, J. Neugebauer, Z. Wang, B. Gault, Machine Learning-Enabled Tomographic Imaging of Chemical Short-Range Atomic Ordering, *Adv. Mater.* 36 (2024). <https://doi.org/10.1002/adma.202407564>.